Available online at www.sciencedirect.com

ScienceDirect

Acta Materialia 85 (2015) 32–41

Acta MATERIALIA

www.elsevier.com/locate/actamat

Thermal dissolution mechanisms of AlN/CrN hard coating superlattices studied by atom probe tomography and transmission electron microscopy

Darius Tytko,* Pyuck-Pa Choi* and Dierk Raabe

Max-Planck-Institut für Eisenforschung GmbH, Max-Planck Str. 1, 40237 Düsseldorf, Germany

Received 28 July 2014; revised 15 October 2014; accepted 3 November 2014

Abstract—AlN/CrN superlattices with a B1 cubic crystal structure and a bilayer period of 4 nm were deposited by reactive radiofrequency magnetron sputtering. The coatings were investigated with respect to their thermal stability and changes in microstructure and chemical composition at 900 °C. The AlN layers show high chemical stability but undergo dissolution by pinching off at grain boundaries. A transformation from cubic to hexagonal AlN with subsequent coarsening at grain boundary triple junctions is observed. In contrast to AlN, the CrN layers show poor chemical stability and their compositions are shifted towards Cr_2N upon annealing in a protective argon atmosphere due to nitrogen loss. However, even after establishing Cr_2N stoichiometry the crystal structure of the layers remains cubic.
© 2014 Acta Materialia Inc. Published by Elsevier Ltd. All rights reserved.

Keywords: AlN/CrN; Hard coatings; Thermal stability; Layer pinch-off; Atom probe tomography

1. Introduction

Thin films based on metal nitrides show superior hardness and wear resistance and are therefore of great interest as protective coating layers [1–5]. Such coatings are important for cutting tool applications, which require high performance as well as extended lifetimes. In order to meet the increasing demands for material properties (e.g. wear, corrosion and oxidation resistance at elevated temperatures) novel material systems need to be explored.

It has been found that nanoscale multilayer hard coatings result in further improvement of hardness as well as corrosion and oxidation resistance as compared to their single-layered counterparts [3,4]. However, in some dry-cutting applications temperatures up to 1000 °C may arise and lead to deterioration of the cutting tool performance. This is because multilayered coatings are susceptible to microstructural changes and layer dissolution at elevated temperatures.

AlN/CrN multilayers are promising materials for cutting tool applications due to their outstanding hardness of ~40 GPa [6,7] and remarkable oxidation resistance [6,8–12]. Although the oxidation and tribological [13,14] resistance of these multilayers have been intensively studied, only a few reports exist on their thermal stability [9,14]. Duh and Tien [9] investigated the thermal stability of AlN/CrN superlattices with a bilayer period of 4 nm by X-ray diffraction (XRD) and transmission electron microscopy (TEM). Their XRD results indicated a preserved multilayer structure after annealing at 850 °C for 1 h in vacuum as well as in air. No structural information could be gathered after annealing at 900 °C for 1 h due to delamination of the coating from the substrate. However, XRD results obtained by Mayrhofer et al. [14] on similar AlN/CrN multilayers showed minor changes of the coating microstructure after exposure to 900 °C for 20 min. Since typical application times of such hard coatings may exceed this limited time frame, we have used atom probe tomography (APT) in conjunction with TEM to study the microstructural changes of AlN/CrN multilayers after isothermal exposure to 900 °C also at longer times.

In general, multilayered materials are susceptible to layer dissolution due to their high density of internal interfaces. At grain boundaries (GBs) at elevated temperatures the layer dissolution mechanism is controlled by interfacial (γ_i) and GB (γ_{GB}) energies, where the layer with the higher γ_{GB}/γ_i ratio is prone to become interrupted at the GB. This effect is often referred as layer "pinch-off" [15–17].

In this work we will reveal that dissolution of the AlN/CrN structure occurs by AlN layer pinch-off at GBs. The resulting nanostructure after exposure to 900 °C consists of nanocrystalline hexagonal AlN and cubic Cr_2N/AlN layers.

* Corresponding authors. Tel.: +49 211 6792 180 (D. Tytko). Tel.: +49 211 6792 167 (P.-P. Choi); e-mail addresses: d.tytko@mpie.de; p.choi@mpie.de

http://dx.doi.org/10.1016/j.actamat.2014.11.004
1359-6462/© 2014 Acta Materialia Inc. Published by Elsevier Ltd. All rights reserved.

2. Experimental

AlN/CrN multilayers were deposited by radiofrequency (RF) magnetron reactive sputtering using Cr (99.9% purity) and AlN (99.9% purity) targets. The latter showed less susceptibility to target poisoning [18,19] and hence more stable deposition rates during reactive sputtering as compared to the metallic Al target. The target power for both Cr and AlN were kept at 100 W.

A polished and cleaned AISI 316 steel was used as the substrate. The base pressure prior to deposition was 2×10^{-7} mbar. After heating up the substrate to 350 °C, Ar gas was introduced and a 200 nm thick Cr adhesion layer was deposited. A gas mixture of Ar (50%) and N_2 (50%) was used for the deposition of a 100 nm thick CrN buffer layer and the AlN/CrN multilayers. The gas pressure for the adhesion, buffer and multilayers was kept at 3×10^{-3} mbar. The multilayers were deposited by rotating the substrate between the individual targets and by using shutters. The movements of the substrate holder as well as the opening times of the shutters were computer-controlled in order to control the individual layer thickness. The resulting total coating thickness was 1.2 μm with a bilayer period of 4 nm for the AlN/CrN multilayers and 1.5 and 2.5 nm thickness for AlN and CrN, respectively. The hardness of the as-deposited coating was measured by means of nanoindentation (Hysitron Triboindenter) and amounted to 31.7 ± 2.3 GPa.

Based on the results of Duh et al. [9] and Mayrhofer et al. [14], we performed isothermal experiments at 900 °C in order to study the temporal evolution of the microstructure.

Samples for annealing were sealed in quartz-glass tubes filled with protective Ar to suppress oxidation. Heat treatments were conducted at 900 °C for 15, 30, 60 and 120 min.

The microstructures of the coatings were observed by conventional TEM as well as scanning TEM (STEM), using a JEOL JEM-2200FS operating at 200 kV.

APT was used to study the microstructure and chemistry of the as-deposited and annealed coatings. The measurements were performed with a local electrode atom probe (LEAP™ 3000X HR, Cameca Instruments) in laser mode (wavelength 532 nm) at 250 kHz pulse frequency, 0.6 nJ laser energy and 0.5% detection rate. The base temperature of the APT samples was kept at ~60 K.

Samples for APT and TEM were prepared using a dual-beam focus ion beam (FIB) microscope (FEI Helios Nanolab 600i) and standard lift-out procedures [20,21]. In the final preparation step, low-kV FIB milling at 5 kV was applied in order to reduce Ga ion implantation and artifacts [22].

3. Results

3.1. TEM

Fig. 1a shows a cross-sectional STEM bright-field (BF) image of the as-deposited coating. Columnar grains can be clearly distinguished, starting from the CrN buffer layer and evolving into the AlN/CrN multilayer region. Selected-area electron diffraction (SAED) performed at one particular columnar grain (marked by the red circle in Fig. 1a) indicates a cubic B1 crystal structure for both the CrN and the AlN layers. Satellite spots around the fundamental reflections (see blue inset in Fig. 1a) indicate the formation of a superlattice and stabilization of the AlN layers to the metastable B1-cubic crystal structure. In the following, the stabilized AlN layers are referred to as c-AlN. A high-angle annular dark-field (HAADF) image taken in STEM mode, which shows the chemical contrast related to the atomic number Z, is presented in Fig. 1b. The bright and dark contrast corresponds to CrN and c-AlN, respectively. Chemically sharp layers with a constant bilayer period of 4 nm can be recognized.

High-resolution (HR) TEM (Fig. 1c) confirms the stabilization of c-AlN and shows coherent interfaces between the c-AlN and CrN layers. Due to their different scattering behaviors, the c-AlN and CrN layers appear with different

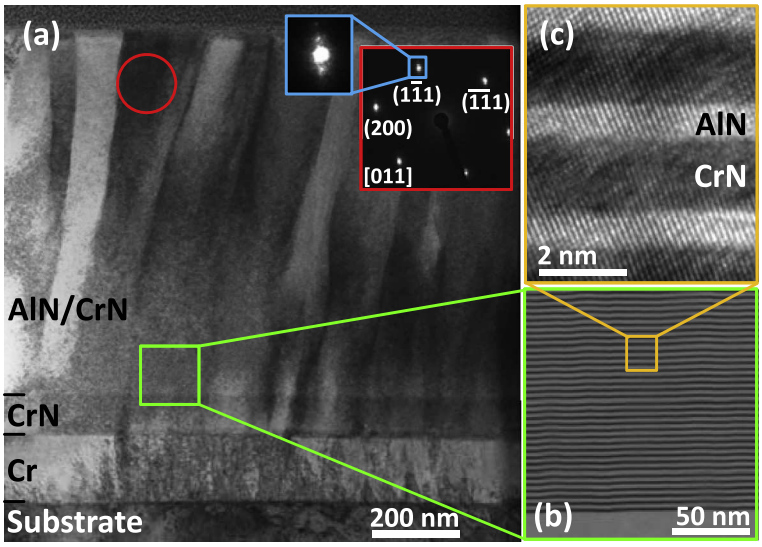

Fig. 1. (a) Cross sectional TEM image of the as-deposited coating, showing columnar grains. The inset displays a SAED pattern from the marked circle. The diffraction pattern reveals fundamental reflections belonging to B1 crystal structure as well as satellite spots; (b) STEM HAADF image from the region marked by the green rectangle in (a). The bright and dark contrast corresponds to CrN and c-AlN, respectively. (c) HR-TEM image showing coherent interfaces. The difference in contrast results from different scattering behavior of CrN (dark contrast) and c-AlN (bright contrast).

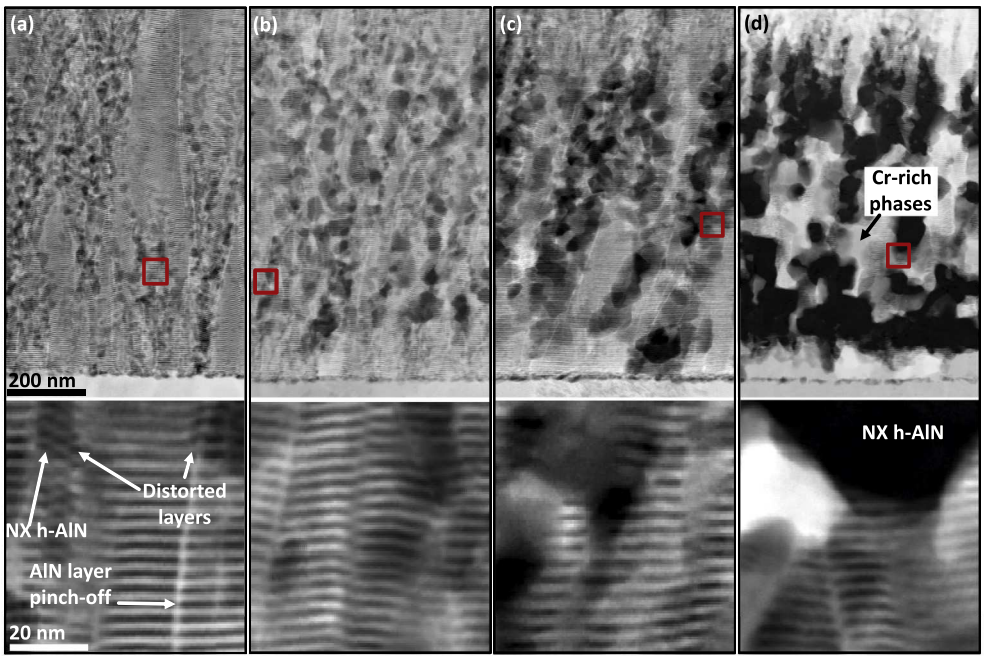

Fig. 2. STEM HAADF images showing the temporal evolution of AlN/CrN multilayers at 900 °C. Bright and dark contrast correspond to CrN and AlN, respectively. Sample annealed for (a) 15 min, (b) 30 min, (c) 60 min and (d) 120 min. The bottom figures show magnified layer structures corresponding to the red squares in the upper figures. Strong distortions of the multilayers surrounding nanocrystalline (NX) h-AlN particles are visible. Pronounced formation of NX h-AlN regions and Cr-rich phases is observed after 120 min of annealing.

contrast and can thus be distinguished from each other. According to Fig. 1c, the layer thickness of c-AlN and CrN is 1.5 and 2.5 nm, respectively.

The STEM HAADF images in Fig. 2a–d show the temporal evolution of the multilayer structure after annealing at 900 °C for 15, 30, 60 and 120 min, where the dark and bright contrast represent AlN and CrN, respectively.

Microstructural changes occur by disconnection of the c-AlN layers at the GBs (see bottom part of Fig. 2a). Such a layer pinch-off was found in all samples annealed at 900 °C.

After the shortest annealing time of 15 min the layer structure is found to disintegrate locally by spheroidization of AlN and subsequent coarsening with increasing annealing time. Multilayers surrounding the coarsened AlN particles are found to be heavily distorted. Fig. 3a shows an in-plane view of the layer structure (parallel to the layers) with small (15-80 nm) and large (80-320 nm) grained regions. AlN (dark contrast region) has preferentially coarsened in regions with smaller grains and thus higher GB densities. A magnified image is presented in Fig. 3b showing CrN-wetted GBs in detail. Coarsened AlN grains are predominantly located at GB triple junctions. However, as a consequence of AlN coarsening the CrN layers are morphologically changed by the redistribution of the Cr atoms and accumulate finally to form separate phases. This is seen most clearly after an annealing time of 120 min, where the resulting microstructure contains strongly coarsened AlN surrounded by Cr-rich phases. TEM observations of the coagulated AlN regions revealed a

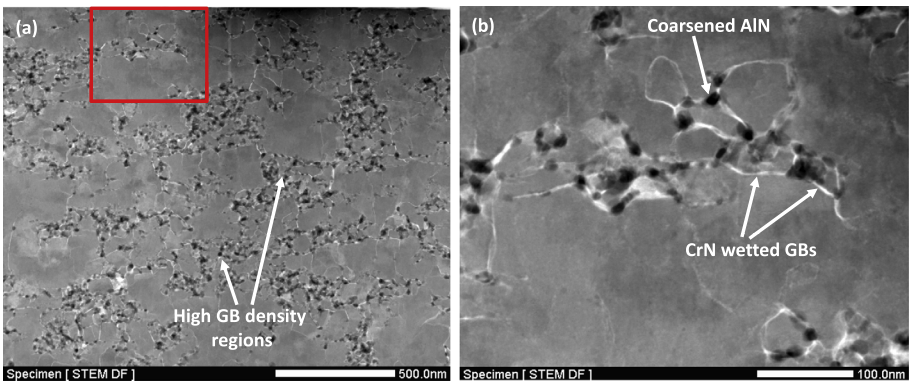

Fig. 3. STEM HAADF image of the longitudinal section providing an in-plane view (parallel to the layers) of the coating annealed for 15 min at 900 °C. The dark and bright contrast corresponds to AlN and CrN, respectively. (a) Top-view of the columnar grain structure showing AlN coarsening in high GB density regions. The GBs are highlighted by CrN wetting; (b) magnified region as marked by the red rectangle in (a) showing CrN wetted GBs as a consequence of c-AlN layer pinch-off, and coarsened AlN forming mainly at GB junctions.

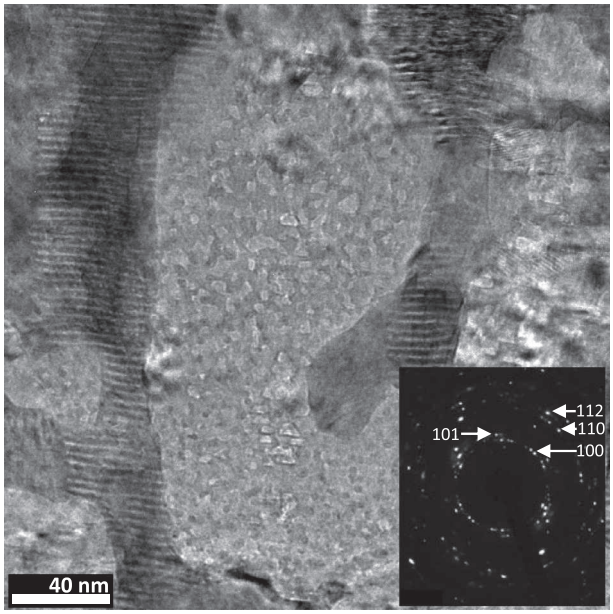

Fig. 4. TEM image of the resulting microstructure after annealing for 120 min. The coagulated AlN region, embedded in multilayer structure, consists of 2.5–15 nm small nanocrystals with hcp structure. The inset shows a diffraction of such a nanocrystalline AlN (NX h-AlN) region.

nanocrystalline hexagonal structure (see Fig. 4). The grain sizes of the nanocrystalline hexagonal AlN (NX h-AlN) range from 2.5 to 15 nm.

Columnar grains in which the multilayers have been preserved can still be found after annealing for 60 min at 900 °C (see Fig. 5a). These grains show a cubic crystal structure similar to the initial structure of the as-deposited coating (see SAED pattern in the inset of Fig. 5a). The Cr adhesion and CrN buffer layers have merged into one layer consisting of hexagonal (space group *P*-31*m*) structured columnar grains (see Fig. 5b and SAED pattern in the inset of Fig. 5b).

3.2. APT

Quantitative analyses of the chemical composition of the AlN/CrN layers were performed by APT. The 3-D atom map of the as-deposited coating (Fig. 6a) and a 1-D concentration profile (Fig. 6b) along the multilayer stack are shown. The slight asymmetry in the concentration peaks is attributed to a difference in the evaporation field of AlN and CrN [23–25] and to inhomogenous evaporation of surface atoms. The latter results in reconstruction artifacts in particular along the direction of analysis. For instance, the transition from a high-field (AlN) to a low-field layer (CrN) leads to a higher reconstructed atomic density at the interface, whereas interfaces between low-field and high-field layers become blurred [26]. Thus, AlN/CrN interfaces yield higher concentration gradients than CrN/AlN interfaces. Bulk mass spectra analyses yield the expected layer stoichiometry of AlN and CrN (see Table 1).

In the following, we will focus on the APT results on the later stages of coarsening, namely after annealing at 900 °C for 60 and 120 min, respectively.

Fig. 7a shows a 3-D atom map of a region in which the multilayer structure is still preserved after annealing at

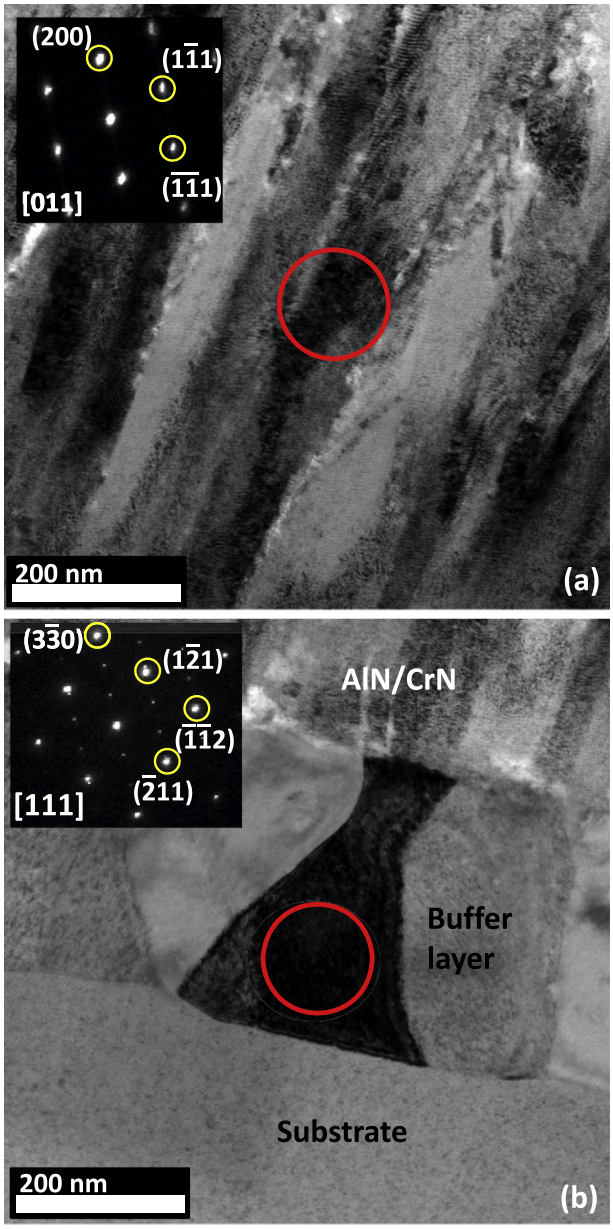

Fig. 5. TEM images of AlN/CrN multilayers annealed for 60 min at 900 °C; (a) columnar grain structure of prevailed multilayers and SAED pattern corresponding to the area marked by the red circle showing B1 cubic crystal structure; (b) merged Cr adhesion and CrN buffer layer after annealing having columnar grains with a P-31 m crystal structure as indicated by the SAED pattern corresponding to the area marked by the red circle.

900 °C for 60 min in Ar atmosphere. The elemental map shows wetting of a columnar GB with CrN as a consequence of c-AlN layer pinch-off. This result is in good agreement with TEM observations (compare bottom image of Fig. 2a). The chemical analysis of the residual multilayers shows an unchanged composition of AlN, but a depletion of N within the CrN layers yielding stoichiometric Cr_2N (Table 1). It is worth noting that even after only 15 min annealing at 900 °C the CrN layers are depleted of N down to the level of a Cr_2N composition. Such a loss in N is a concequence of the low N partial pressure during annealing. Local analysis of the wetted GB shows further

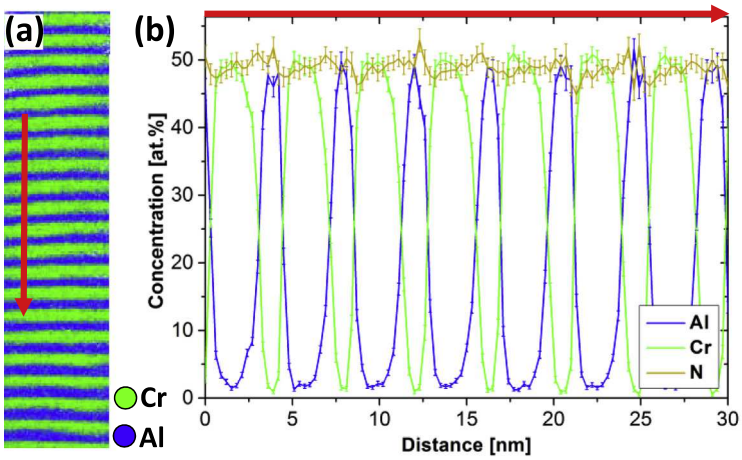

Fig. 6. (a) 3d atom map of the as-deposited AlN/CrN multilayers; (b) 1-D concentration profile along the red arrow in (a).

Table 1. Chemical composition of as-deposited coating and coating annealed at 900 °C for 60 min in Ar. The impurities include C, Fe, Ni, Cu and B partly stemming from the steel substrate after annealing.

Condition	Region	Cr [at.%]	Al [at.%]	N [at.%]	O [at.%]	Impurities [at.%]
As-deposited	AlN	1.2 ± 0.2	49.6 ± 1.2	48.2 ± 1.2	1.0 ± 0.1	0.03 ± 0.01
	CrN	49.9 ± 0.4	2.4 ± 0.6	47.3 ± 0.8	0.4 ± 0.1	0.02 ± 0.01
900 °C/60 min	AlN layers	2.0 ± 1.8	49.0 ± 1.3	48.0 ± 1.4	1.0 ± 0.2	0.11 ± 0.08
	AlN phases	0.2 ± 0.14	50.7 ± 0.2	47.1 ± 0.5	1.7 ± 0.1	0.26 ± 0.14
	Cr_2N layers	62.9 ± 1.3	5.2 ± 0.7	31.6 ± 1.8	0.2 ± 0.04	0.03 ± 0.01
	Cr_2N layers close to GB	59.0 ± 0.8	6.0 ± 0.6	34.9 ± 0.1	–	–
	Cr_2N at GB	69.4 ± 0.6	1.9 ± 0.2	28.7 ± 0.4	–	–
	Buffer layer	72.1 ± 0.8	–	27.9 ± 0.8	–	–

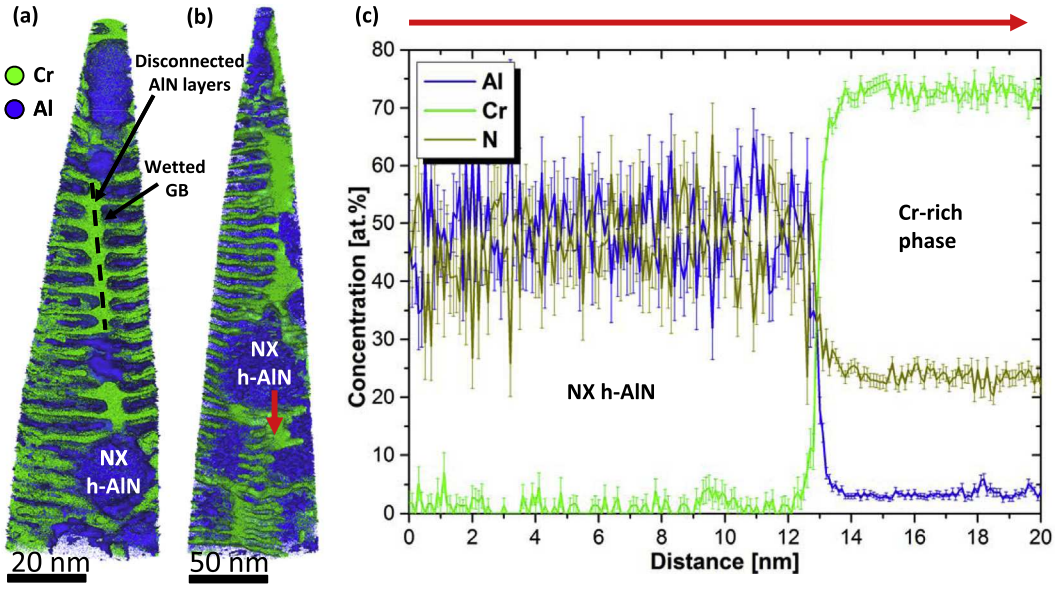

Fig. 7. (a) 3d atom maps of the coating annealed for 60 min at 900 °C (from the central multilayer region); disconnected AlN layers and spheroidized AlN are visible at a GB; (b) coarsened AlN and adjoining Cr accumulations; (c) 1-D concentration profile along the red arrow in (b) across the interface of coarsened AlN and a Cr-rich region. The composition of the Cr enriched phase shows up to 75 and 25 at.% of Cr and N, respectively. For the sake of illustration, iso-concentration surfaces of 45 at.% Cr and 35 at.% Al are plotted in order to highlight the microstructures in (a) and (b).

depletion of N by ~6 at.%, but an enrichment of Cr by 10 at.% as compared to the surrounding Cr_2N layers.

Additionally, O impurities are detected, which are preferentially located inside the AlN. The exact compositions of the separate phases and layers are listed in Table 1.

The 3-D atom maps in Fig. 7a and b reveal that spheroidization and coarsening of AlN mainly occur at the GB triple junctions, which is consistent with TEM observations (see Fig. 3). The coarsened AlN exhibits a similar composition as the layered c-AlN.

Fig. 7b shows a 3-D atom map containing a large number of coarsened AlN. Pile-ups of Cr atoms between spheroidized AlN regions can be detected. The composition of this Cr-enriched phase is $Cr_{0.74}N_{0.23}$ with ~3 at.% additional impurities (Al, Fe, Ni and Cu) partly stemming from the steel substrate. The content of Al within the Cr-rich phase in the concentration profile (Fig. 7c) is overestimated by ~2 at.% due to a peak overlap in the bulk mass spectrum of Al^+ and the Cr^{2+} isotope at 26.98 and 26.97 Da, respectively. This overlapped peak is assigned to Al^+, which is correct for the AlN, but yields in turn a slightly overestimated Al concentration within the CrN when plotting concentration profiles (see Fig. 7c).

The coating annealed at 900 °C for 120 min exhibits a strongly granular microstructure with NX h-AlN grains surrounded by Cr-rich phases. A 3-D atom map is presented in Fig. 8 which shows coarsened NX h-AlN and Cr-rich regions as well as some residual layer structures in the bottom region. Both the Cr-rich phase surrounding NX h-AlN and residual multilayers show identical compositions as the sample annealed for 60 min (Fig. 7b). A different perspective of Fig. 8a is shown in Fig. 8c. The slice view visualizes B segregation to GBs in the NX h-AlN region. The B content (stemming from the substrate) in the NX h-AlN regions formed after 120 min of annealing is 0.2 ± 0.09 at.%.

4. Discussion

4.1. Stability of the nanoscale multilayer structure and layer dissolution mechanisms

The epitaxial stabilization of a metastable c-AlN layer instead of h-AlN, which is in fact the equilibrium phase, is induced by coherency strains to the seed layer located underneath. While nucleating on a series of alternated nanolayers the stabilized c-AlN is in a different strain state than a comparable bulk material would be [27]. In general, properties such as the individual layer thickness, bilayer period and lattice parameter influence the strain state and thus the epitaxial stabilization of a layer [27–29]. Upon exceeding a critical epitaxial layer thickness the stabilization effect vanishes, resulting in the equilibrium crystal structure. Chawla et al. [30] calculated a critical theoretical thickness of 3.8 nm for the case of c-AlN on CrN. However, it is generally known that sputter-deposition techniques induce a high density of defects, which can profoundly influence the stress states of a thin film [31]. Thus, the stress level may change the critical c-AlN layer thickness depending on the sputter-deposition method and parameters. In our experiments, the critical c-AlN layer thickness was ~2 nm for a bilayer period of 4 nm. As shown by Mayrhofer et al. [14], AlN/CrN superlattices exhibit the highest hardness values at layer ratios of 1:2 for AlN and CrN, respectively. Hence, we chose a bilayer period of 4 nm with an AlN layer thickness of ~1.5 nm in order to achieve epitaxial stabilization and high coating hardness. As a result of the epitaxial stabilization, individual layers grow with identical crystal structure and coherent interfaces, leading to a columnar microstructure [32].

After thermal exposure, interruptions of the AlN layers at the columnar GBs are observed (see Figs. 2a and 3). Such GB pinch-off behavior (and hence wetting of the

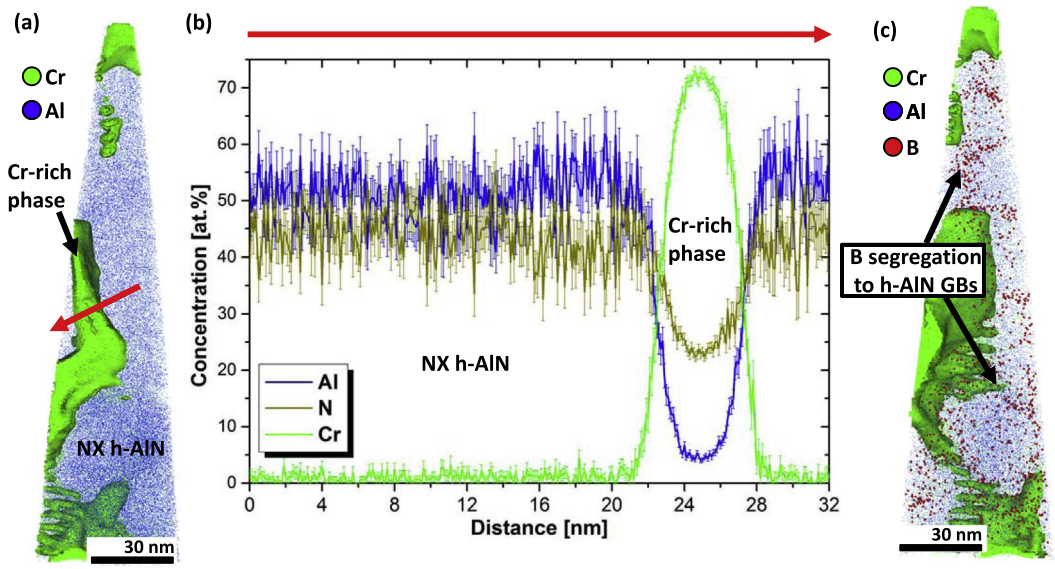

Fig. 8. (a) AlN/CrN multilayer after annealing at 900 °C for 120 min. Layer structure is mainly dissolved leading to formation of separate AlN and Cr-rich phases; (b) concentration profile along the red arrow in (a) showing stoichiometric AlN and a Cr-rich phase. For better clarity, an iso-concentration surface of 45 at.% Cr is plotted to highlight Cr-rich regions (a); (c) different perspective of (a) showing segregation of B to NX h-AlN GBs.

GB by capillary forces) in multilayered coatings results from the competition between GB energy (γ_{GB}) and the interface energy (γ_i) [16,17,33]. A schematic illustration of the AlN layer pinch-off at the GBs is presented in Fig. 9a–c. The left-hand side of Fig. 9a shows a GB triple junction of the as-deposited coating with a corresponding cross-sectional view of the layer structure on the right-hand side. The cross-sectional views refer to the red dashed lines in the images on the left. Layers with a higher γ_{GB} start to develop grooves at the GB at elevated temperatures (Fig. 9b). The relation between the grooving angle (Θ), γ_{GB} and γ_i is given by $\cos\Theta = \gamma_{GB}/2\gamma_i$ [17]. Driven by

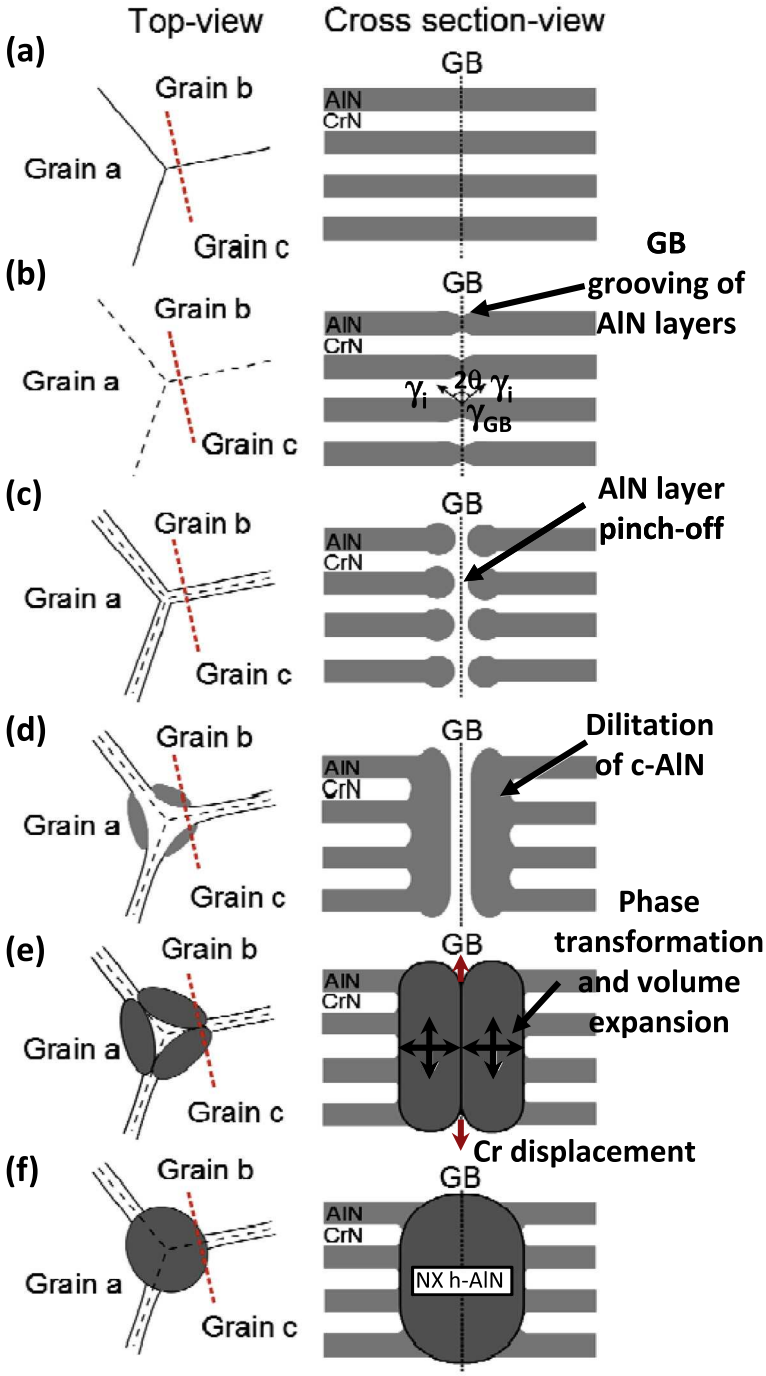

Fig. 9. Schematic of AlN layer pinch-off and AlN coarsening at GB triple junction. The left hand side images show the in-plane view (parallel to multilayers); the images on the right hand side show the multilayer cross section along the dashed red line indicated in the left hand side images. (a) Initial GB triple junction configuration (top-view left) and multilayer arrangement (right); (b) GB grooving of AlN layers; (c) disconnection at GB junctions lead to tapering of AlN layers (left) and AlN pinch-off with spheroidized layer termination points along the GB (right hand side); (d) These tapered AlN layers round-off (left) and the retracted material dilates along the layer stack by connection of the spheroid termination points (right); (e) Crystallographic transformation of c-AlN to h-AlN with accompanied volume expansion leads to the connection of the AlN crystals and Cr displacement of the GB; (f) Coarsened AlN at the GB junction consisting of multiple grains (NX h-AlN).

the minimization of free interfacial energy in the system the layers with the higher γ_{GB} are pinched-off upon annealing. Once the AlN layers become discontinuous, the system lowers the interfacial energy by forming round layer termination points [34,35] (Fig. 9c). Note that γ_{GB} depends on the grain misorientation, and thus not every GB is prone to undergo layer pinch-off [15]. Nevertheless, the interruption of the continuity of the AlN layers at the GBs is a strong indication for a higher GB energy as compared to the GB energy of the CrN layers. To the authors' knowledge, γ_{GB} values for CrN and c-AlN are not available. However, relative trends for γ_{GB} can be predicted from surface energies. For instance, CrN and c-AlN with (100)-oriented facets are reported to have surface energies of 0.74 [36] and 1.33 J/m^2 [30], respectively. The higher surface energy of c-AlN is in agreement with the observed c-AlN layer pinch-off at GBs.

In addition to the AlN layer pinch-off, coarsened NX h-AlN was mainly observed at GB triple junctions (see Figs. 2a and 3). Hence, the following formation mechanism of AlN at these special locations is proposed (Fig. 9d–f). The AlN layers pinch-off at triple junctions leading to tapered layers pointing towards the GB intersection (illustrated at left side of Fig. 9c). Subsequently, the termination points of the AlN layers change into rounded shapes in order to minimize the interfacial area and energy owing to the capillary driving force (see left picture in Fig. 9d). The spheroidized termination points coarsen and become connected (see right side of Fig. 9d). Monte Carlo simulations conducted by Bobeth et al. [35] showed that even at a temperature of 600 °C such layer interconnections parallel to the GB are completed within seconds in the case of Cu/Co multilayers. Thus, the in situ experimental observation of such a coarsening process may be difficult. For the studied AlN/CrN multilayer system this coarsening process significantly progresses even after annealing only for 15 min at 900 °C. Once the AlN layers are interconnected close to the GBs the epitaxial stabilization hence no longer prevails and phase transformation of c-AlN into the thermodynamically stable h-AlN occurs (Fig. 9e). This transformation is reported to be accompanied by a volume expansion of ~26% [37]. As a result, the individual differently oriented particles of grains a, b and c (Fig. 9e) can come into contact and form a nanocrystalline AlN region. Due to the high chemical stability of AlN the Cr atoms at the wetted GBs are subsequently displaced along the GBs and form overstoichiometric Cr_2N (see Table 1). In addition to coagulation of nanocrystalline h-AlN particles, the large volume expansion during transformation from c-AlN to h-AlN can induce plastic distortions (see bottom images of Fig. 2) and defects in the surrounding AlN/CrN multilayers. Consequently, additional grain boundaries in the adjacent c-AlN layers can be formed, which in turn would trigger the pinch-off effect and the subsequent formation h-AlN. Plastic deformation in the enclosed multilayer structure can also lead to the interconnection of c-AlN layers followed by h-AlN transformation.

Even though only the final state could be observed due to the prolonged annealing times imposed, the proposed process provides a reasonable explanation for the formation of NX h-AlN at GB junctions.

In particular, regions with a high number density of GBs (see Fig. 3a) agglomerate to extended nanocrystalline regions after prolonged annealing (see Fig. 4). Such NX h-AlN regions contain a significant number of GBs as well as incoherent h-AlN/CrN and h-AlN/c-AlN outer interfaces. To date, interfacial energies of c-AlN/CrN and h-AlN/CrN or h-AlN/c-AlN have not been reported in the literature. However, due to the same crystal structure and similar lattice parameter of TiN (4.24 Å [38]), CrN (4.14 Å [39]) and c-AlN (4.12 Å [38]) we approximate the interfacial energies of coherent c-AlN/CrN by the interfacial energy of c-AlN/TiN (~1 J/m^{-2} [40]) and the interfacial energies of the incoherent h-AlN/CrN and h-AlN/c-AlN interfaces by the interfacial energy of h-AlN/TiN (~3 J/m^{-2} [40]). The GB energies of h-AlN may be approximated by h-AlN surface energies, which range from 2.3 to 5.8 J/m^{-2} depending on the orientation of the surface facet [30]. In general, GB energies are lower than the corresponding surface energies (e.g. factor of ~3 for the case of Cu [41]). Moreover, the observed B segregation to the h-AlN GBs (see Fig. 8c) is expected to further lower the GB energies. Such segregation of solute elements is known to inhibit grain coarsening and lead to stable structures of nanocrystalline materials [42,43].

The existence of a nanocrystalline structure of h-AlN grains suggests lower GB energies as compared to the h-AlN/CrN interfacial energies. The NX h-AlN regions are found to coagulate in order to reduce the high interfacial energy of the hexagonal/cubic interface and thus the total free energy of the system.

The process of progressive coagulation of AlN grains displaces the residual Cr atoms, which accumulate and form Cr-rich phases (compare bright contrast phases in Fig. 2d).

The residual layer structure in all annealing stages shows stoichiometric compositions of AlN and Cr_2N. The chemically unstable CrN layers release N_2 at 900 °C until a stable composition of Cr_2N is reached. TEM diffraction of such multilayer regions proved the presence of cubic Cr_2N layers (c-Cr_2N) with a B1 crystal structure (see Fig. 5a). As mentioned above, the initial c-AlN layers became epitaxially stabilized to a B1 crystal structure by coherency strains to the CrN seed layers. It is assumed that these strains are still present within the multilayer structure and prevent the formation of the hexagonal Cr_2N crystal structure. Based on the observations, the resulting c-Cr_2N layers are believed to contain a high number of nitrogen vacancies, which result in the reduction of the lattice parameter [44]. Besides the free volume at GB triple junctions, such lattice shrinkage may facilitate the volume expansion of c-AlN during phase transformation to h-AlN.

4.2. Chemical analysis of the layers

The N concentrations of as-deposited c-AlN and CrN layers, measured by APT, are 48.1 ± 1.2 and 47.1 ± 0.5 at.%, respectively. The slightly lower concentration of N within CrN is believed to originate from molecular evaporation due to a higher metal–nitrogen binding energy (396.8 eV [45]) as compared to AlN (73.8 eV [46]). In such an evaporation mode molecular dissociation processes may occur, which result in multiple detector hits highly correlated in space and time. The narrow impact sites at the detector may lead to undistinguishable signals and thus loss of preferentially dissociated species. Further, neutral species (e.g. N_2) may be produced by dissociation processes that are not considered in the mass-to-charge spectrum [47]. Both processes can lower the detectability of N in materials with predominant molecular evaporation. Moreover, a

slight mixing of Al and Cr in the as-deposited state, which is detected by APT, is ascribed to ballistic processes during sputter-deposition.

After exposure of the coatings to 900 °C the CrN layers start to lose N, resulting in stoichiometric Cr_2N. It is well known that the thermodynamic stability of CrN is limited to a critical temperature at which release of N_2 induces the formation of Cr_2N. Further loss of nitrogen leads to decomposition of Cr_2N to body-centered cubic Cr [39,48,49]. Ernst et al. [39] determined the onset temperature of 925 °C for N_2 release in CrN coatings annealed in Ar atmosphere. As shown by Lu and Chen [50], the critical temperature for transformation of CrN into Cr_2N may be lowered by stress relaxation processes when sputter-induced defects undergo recovery [51]. In their experiments the formation of Cr_2N was observed for temperatures between 500 and 650 °C. Thus, the observed N escaping at 900 °C in Ar atmosphere is conceivable. One should also note that stress states play a major role in our superlattice structure, since the layers retain their initial crystal structure despite the fact that N is released within the CrN.

In contrast to CrN, AlN shows high chemical stability by maintaining its stoichiometric composition at all annealing times (Table 1). Coarsening of AlN leads to pile-ups of Cr between NX h-AlN regions (see Fig. 8). As a result, a Cr-rich $Cr_{0.75}N_{0.25}$ phase is formed. According to the phase diagram for the Cr-N system, the lower limit for N concentration in β-Cr_2N at 1292 °C is given by 25.07 at.% [52]. This value matches well with the measured N content in the Cr-rich phase after 60 and 120 min of annealing (compare Figs. 7 and 8). Due to the smaller NX h-AlN volume fraction in the coatings annealed for 15 and 30 min no Cr-rich phase has been detected by APT. Instead, excess Cr was found to be enriched at GBs.

The wetted GB in Fig. 8a is located close to a triple junction as revealed by the 3-D atom map. The chemistry of this GB yields ~10 at.% higher Cr concentrations as compared to the adjacent Cr_2N layers. Two mechanisms may be responsible for such Cr excess. On the one hand, the formation of NX h-AlN at the GB triple junction may redistribute the displaced Cr atoms preferentially onto the adjacent GBs (see schematic in Fig. 9e). On the other hand, the large diffusion coefficient on GBs results in a fast diffusion path for N release along the columnar GBs. As a result, a lower concentration of N (and thus a higher concentration of Cr) at the GB compared to the surrounding layers is expected.

In order to investigate the influence of the Ar atmosphere on the N_2 release in the coatings, annealing experiments at 900 °C in flowing N_2 gas were also conducted. The results show no striking differences regarding the microstructure and chemical composition of the coatings annealed in Ar and N_2, respectively. The latter is a consequence of the high partial pressure of N, which is needed to stabilize the stoichiometric CrN. In particular, AlN showed again good chemical stability by maintaining its stoichiometric composition. The N loss in the coating annealed in N_2 was found to be less pronounced and the Al content within the CrN layers was higher compared to that of the CrN layers annealed in Ar. For instance, the CrN layers showed a chemical composition of 45.7 ± 1.2, 41.1 ± 1.7 and 13.9 ± 0.8 at.% of Cr, N and Al, respectively. The higher solubility of Al within the CrN layers is a subject of ongoing research.

5. Conclusion

AlN/CrN multilayers with bilayer periods of 4 nm were deposited by reactive RF magnetron sputtering. The resulting superlattices have B1 cubic crystal structure due to epitaxial stabilization of the AlN layers.

Isothermal annealing experiments at 900 °C in Ar atmosphere were performed in order to study the dissolution mechanisms and kinetics of the coating microstructure. The c-AlN layers are found to pinch-off at GBs. This behavior indicates a higher GB energy of c-AlN layers as compared to the CrN layers. Layer pinched-off GB junctions provide preferential sites for the formation of NX h-AlN. With progressive annealing time (15–120 min) h-AlN grains coarsen and coagulate with nearby AlN grains. As a result Cr is redistributed and accumulated around the NX h-AlN. Thus, after 120 min of annealing a considerable volume fraction of separate NX h-AlN and Cr-rich phases is present.

Furthermore, loss of N within the chemically unstable CrN layers is found to occur even after the shortest annealing time of 15 min, resulting in Cr_2N layer stoichiometry. Regardless of the chemical compositions of both the AlN and Cr_2N layers, the crystal structure remains cubic.

In conclusion, our results show that the c-AlN layers are the critical phase regarding layer stability due to layer pinch-off and formation of NX h-AlN at GB junctions. Hence, an improved thermal stability of AlN/CrN superlattices may be achieved with microstructures containing a low density of GBs and/or by lowering of the GB energy of c-AlN, e.g. by decoration with solute elements.

Acknowledgment

The authors gratefully acknowledge funding of this work by the German Research Foundation (DFG) (Contract CH 943/1-1).

References

[1] P.H. Mayrhofer, C. Mitterer, L. Hultman, H. Clemens, Prog. Mater. Sci. 51 (2006) 1032.
[2] S. PalDey, S.C. Deevi, Mater. Sci. Eng. A Struct. 342 (2003) 58.
[3] S. Veprek, S. Reiprich, Thin Solid Films 268 (1995) 64.
[4] H. Holleck, V. Schier, Surf. Coat. Technol. 76–77 (1995) 328.
[5] C. Subramanian, K.N. Strafford, Wear 165 (1993) 85.
[6] J.-K. Park, Y.-J. Baik, Surf. Coat. Technol. 200 (2005) 1519.
[7] J. Lin, J.J. Moore, B. Mishra, M. Pinkas, W.D. Sproul, Surf. Coat. Technol. 204 (2009) 936.
[8] U. Bardi, S.P. Chenakin, F. Ghezzi, C. Giolli, A. Goruppa, A. Lavacchi, et al., Appl. Surf. Sci. 252 (2005) 1339.
[9] S.-K. Tien, J.-G. Duh, Thin Solid Films 494 (2006) 173.
[10] S.-K. Tien, J.-G. Duh, J.-W. Lee, Surf. Coat. Technol. 201 (2007) 5138.
[11] B.S. Kim, G.S. Kim, S.Y. Lee, B.Y. Lee, Surf. Coat. Technol. 202 (2008) 5526.
[12] S.-K. Tien, C.-H. Lin, Y.-Z. Tsai, J.-G. Duh, J. Alloys Compd. 489 (2010) 237.
[13] A. Rojo, J. Solís, J. Oseguera, O. Salas, R. Reichelt, J. Mater. Eng. Perform. 19 (2010) 421.
[14] M. Schlögl, J. Paulitsch, P.H. Mayrhofer, Surf. Coat. Technol. 240 (2014) 250.
[15] A.C. Lewis, D. Josell, T.P. Weihs, Scr. Mater. 48 (2003) 1079.
[16] D. Josell, W.C. Carter, J.E. Bonevich, Nanostruct. Mater. 12 (1999) 387.

[17] J.C.M. Kampe, T.H. Courtney, Y. Leng, Acta Metall. 37 (1989) 1735.
[18] L. Combadiere, J. Machet, Surf. Coat. Technol. 82 (1996) 145.
[19] D. Depla, R. De Gryse, Surf. Coat. Technol. 183 (2004) 196.
[20] G.B. Thompson, M.K. Miller, H.L. Fraser, Ultramicroscopy 100 (2004) 25.
[21] M. Schaffer, B. Schaffer, Q. Ramasse, Ultramicroscopy 114 (2012) 62.
[22] K. Thompson, D. Lawrence, D.J. Larson, J.D. Olson, T.F. Kelly, B. Gorman, Ultramicroscopy 107 (2007) 131.
[23] F. Vurpillot, D. Larson, A. Cerezo, Surf. Interface Anal. 36 (2004) 552.
[24] P.-P. Choi, I. Povstugar, J.-P. Ahn, A. Kostka, D. Raabe, Ultramicroscopy 111 (2011) 518.
[25] E.A. Marquis, B.P. Geiser, T.J. Prosa, D.J. Larson, J. Microsc. 241 (2011) 225.
[26] F. Vurpillot, A. Cerezo, D. Blavette, D.J. Larson, Microsc. Microanal. 10 (2004) 384.
[27] I.W. Kim, Q. Li, L.D. Marks, S.A. Barnett, Appl. Phys. Lett. 78 (2001) 892.
[28] Q. Li, I.W. Kim, S.A. Barnett, L.D. Marks, J. Mater. Res. 17 (2002) 1224.
[29] D. Chen, X.L. Ma, Y.M. Wang, Acta Mater. 53 (2005) 5223.
[30] V. Chawla, D. Holec, P.H. Mayrhofer, J. Phys. D (2013) 46.
[31] A.J. Perry, J.A. Sue, P.J. Martin, Surf. Coat. Technol. 81 (1996) 17.
[32] A. Mazor, D.J. Srolovitz, P.S. Hagan, B.G. Bukiet, Phys. Rev. Lett. 60 (1988) 424.
[33] D. Josell, S.R. Coriell, G.B. McFadden, Acta Metall. Mater. 43 (1995) 1987.
[34] G. Sharma, R.V. Ramanujan, G.P. Tiwari, Acta Mater. 48 (2000) 875.
[35] M. Bobeth, M. Hecker, W. Pompe, C.M. Schneider, J. Thomas, A. Ullrich, et al., Z. Metall. 92 (2001) 810.
[36] D. Siegel, L. Hector, J. Adams, Phys. Rev. B (2003) 67.
[37] M. Schlögl, J. Paulitsch, J. Keckes, P.H. Mayrhofer, Thin Solid Films 531 (2013) 113.
[38] A. Hörling, L. Hultman, M. Odén, J. Sjölén, L. Karlsson, Surf. Coat. Technol. 191 (2005) 384.
[39] W. Ernst, J. Neidhardt, H. Willmann, B. Sartory, P.H. Mayrhofer, C. Mitterer, Thin Solid Films 517 (2008) 568.
[40] A. Madan, I.W. Kim, S.C. Cheng, P. Yashar, V.P. Dravid, S.A. Barnett, Phys. Rev. Lett. 78 (1997) 1743.
[41] R. Chattopadhyay, Surface Wear: Analysis, Treatment, and Prevention, Materials Park, OH; ASM International, 2001.
[42] D.L. Beke, J. Appl. Phys. 95 (2004) 4996.
[43] R. Kirchheim, Acta Mater. 50 (2002) 413.
[44] A. Abdulkadhim, T. Takahashi, D. Music, F. Munnik, J.M. Schneider, Acta Mater. 59 (2011) 6168.
[45] A. Conde, A.B. Cristóbal, G. Fuentes, T. Tate, J. de Damborenea, Surf. Coat. Technol. 201 (2006) 3588.
[46] J. Chakraborty, S. Mukherjee, P.M. Raole, P.I. John, Mater. Sci. Eng.: A 304–306 (2001) 910.
[47] D.W. Saxey, Ultramicroscopy 111 (2011) 473.
[48] P.H. Mayrhofer, F. Rovere, M. Moser, C. Strondl, R. Tietema, Scr. Mater. 57 (2007) 249.
[49] F. Rovere, D. Music, S. Ershov, M.T. Baben, H.G. Fuss, P.H. Mayrhofer, J.M. Schneider, J. Phys. D (2010) 43.
[50] H.-Y. Chen, F.-H. Lu, J. Mater. Sci. Lett. 22 (2003) 817.
[51] P.H. Mayrhofer, H. Willmann, A.E. Reiter, Surf. Coat. Technol. 202 (2008) 4935.
[52] W. Mayr, W. Lengauer, P. Ettmayer, D. Rafaja, J. Bauer, M. Bohn, JPE 20 (1999) 35.